dimensional domain. In practice, applied fields are three-dimensional, especially for small, unguarded electrodes; unless the test domain is carefully chosen to be uniform in the third dimension, the 2-D image which results will reflect the 3-D nature of the excitation field. (While three-dimensional current flow has been used for some elementary cases, including the vertical bubble-column flows in this work, full three-dimensional EIT reconstruction would require impractical amounts of computational effort and resources.) Another common simplification involves representing the conductivity by a piecewise constant function – *e.g.*, a constant within each element of a finite-element mesh. This approach is not followed here; instead, the conductivity is represented as a global function of position and of several conductivity parameters. By using a global conductivity function, regularization is implicitly included in the solution procedure. It is also assumed in EIT that the impedance distribution within the domain does not change significantly over time while voltage projections are acquired. To satisfy this assumption, EIT systems must acquire projections rapidly, on time scales shorter than the characteristic time scales of multiphase flows. In the vertical multiphase flows examined in this report, this cannot be achieved, so the uncertainty introduced by temporal averaging of voltages prior to reconstruction must be quantified. This consideration is discussed in more detail later in this report.

More information on EIT theory and the development of EIT systems for the study of multiphase flows may be found in Dickin *et al.* (1993); Jones *et al.* (1992, 1993, 1994); and Ceccio and George (1996).

3.2. System Description

3.2.1. EIT Hardware and Electronics

A block diagram of the Sandia/Michigan EIT system (Torczynski *et al.*, 1997; George *et al.*, 1998b) is shown in Figure 3.2. The system hardware consists of an electrode array; a signal generator; a voltage-controlled current source; multiplexers connecting the electrode array to the current source, current ground, and measurement electronics; an instrumentation amplifier and phase-sensitive demodulators; a low-pass filter to eliminate high-frequency components from the demodulated signals; and a Data Translation® model DT2839 data acquisition card. The data acquisition card contains a 12-bit analog-to-digital converter that measures the demodulated signal components and a digital controller that can be used to select electrodes for current injection, current ground, and voltage measurement. The card also acts as an interface to a Pentium PC that operates the entire system. A photograph of the system is shown in Figure 3.3; a complete circuit diagram of the EIT package appears in Appendix A.

A variety of schemes have been employed in EIT systems to acquire voltage projection sets. In principle, voltages need only be measured across the two electrodes used to inject and withdraw current, and different combinations of injection and withdrawal electrodes will produce the complete set of voltages needed in reconstruction. Systems that employ this approach are referred to as "two-port" systems. In practice, however, the contact impedances at the interfaces between the two current-bearing electrodes and the domain will cause significant voltage drops

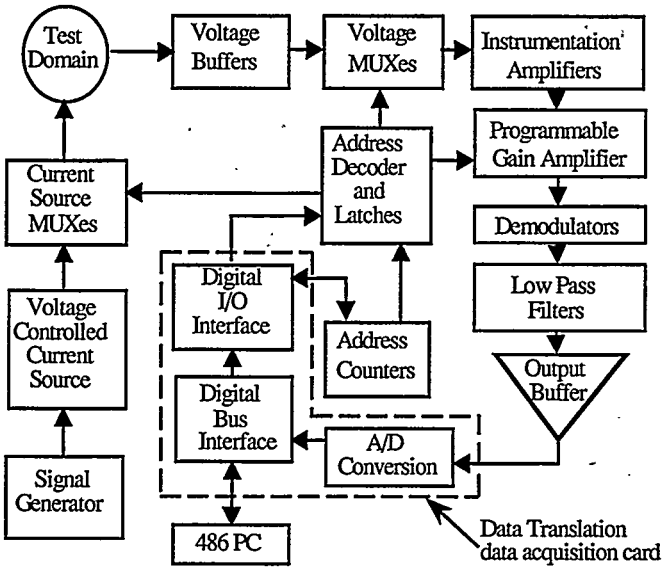

Figure 3.2. Block diagram of the Sandia/Michigan EIT system.

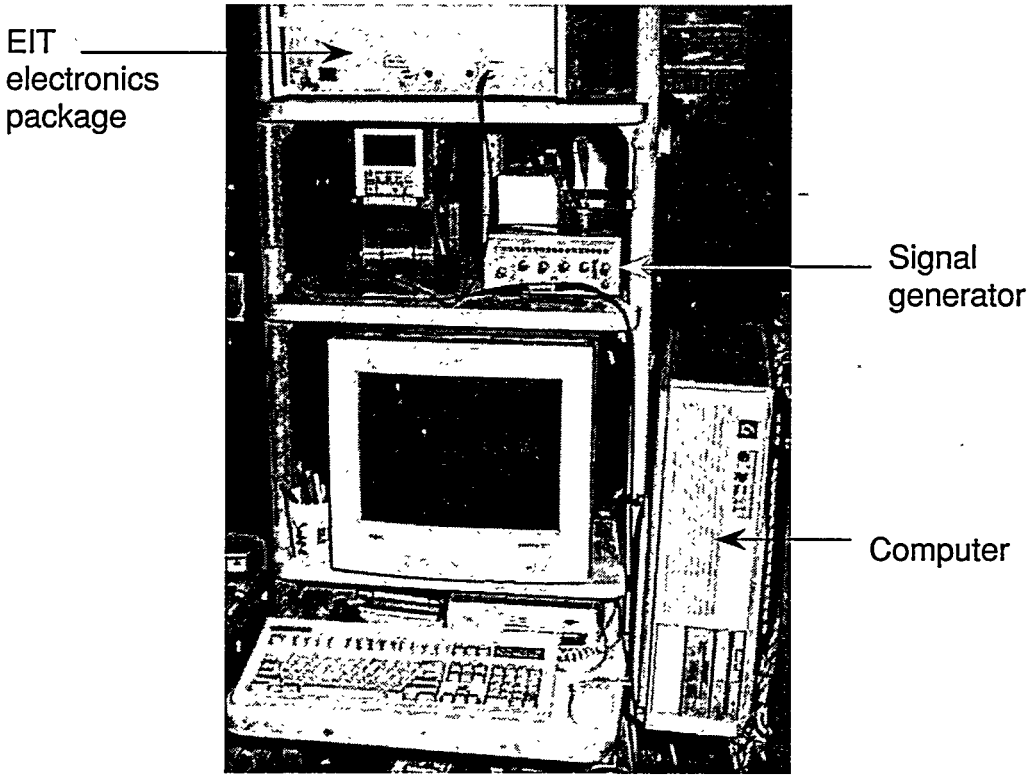

Figure 3.3. Photograph of the Sandia/Michigan EIT system.

across the interfaces and introduce errors in the reconstruction. Furthermore, to acquire a set of projections with a good signal-to-noise ratio, significant current should be induced within the entire domain to produce measurable voltage changes at the boundary, but two-port systems can concentrate current near the boundary and leave the interior of the domain unprobed.

Consequently, "four-port" systems have been devised that use two electrodes to inject and withdraw current and two other electrodes to measure differences in boundary voltages.

The Sandia/Michigan EIT system is a four-port system that injects a controlled current through one electrode, grounds a second electrode to withdraw the current, and measures voltages at all electrodes in sequence relative to the ground electrode. For completeness, a "projection set" consists of measurements at all N electrodes for each injection and ground combination, with a total of $N^2(N-1)/2$ voltage measurements. Note that this is a factor of N greater than the number of independent pieces of information, M (Eq. 3.3); the extra information is used to reduce the impact of noise on the reconstructions. The measurement at the injection electrode is not used in reconstructions in the Sandia/Michigan system because of the possible error from contact impedance discussed above (Torczynski *et al.*, 1996a, 1997).

The domain is excited with a 50-kHz AC electric field. At this frequency, the resistive component of impedance dominates for the air-water and polystyrene-water flows considered here (Ceccio and George, 1996), a fact which will be demonstrated in Section 3.2.2. At the head of the excitation circuitry is a Hewlett-Packard Model 3312A function generator that produces a stable, low-distortion 50-kHz sine wave of peak-to-peak magnitude 1 V. This magnitude was chosen based on the resistance and transient behavior of the multiplexers used to select electrodes for current injection and voltage measurement. The signal is sent through a buffer (a single operational amplifier, referred to hereafter as an "op-amp") to a voltage-controlled current source (VCCS, see Appendix A) that creates an injection current proportional to the voltage of the reference sine wave. In the present configuration, an input of 1 V p/p yields a current output of approximately 125 μA rms.

To keep the current amplitude stable over a wide range of domain impedances, the VCCS employs two op-amps in a positive feedback design: an OP42 that acts as the heart of the current source, and a National Semiconductor model LH0032, which buffers the current and provides positive feedback to the OP42. The output of the VCCS is AC coupled to prevent the transmission of a polarizing DC current to the electrodes. The conductivity of the domain must be checked and adjusted as needed before experiments, since high conductivity can cause saturation of the VCCS. A Burr-Brown model INA110 instrumentation amplifier connected to the sensing resistor of the VCCS provides a voltage proportional to the current output; this voltage may be measured by the data acquisition board to monitor the current output for stability or signs of saturation.

The reference sine wave is sent not only to the VCCS but also to phase-sensitive demodulators for use in domain voltage measurements. An all-pass filter also uses the reference sine wave to generate a quadrature reference for measurement purposes. The all-pass filter may be tuned with two potentiometers to ensure that the quadrature reference is 90º out of phase with, and has the same magnitude as, the original carrier reference.

The electrode array is connected to the VCCS and current ground via two Analog Devices model MUX16 analog multiplexers ("muxes" for short). Multiplexers are also used to connect the electrode array to the differential amplifier used to measure electrode voltages. Latch commands issued to the muxes determine which electrodes are selected for current injection, grounding, and voltage measurement, and the speed of these commands is the largest

factor influencing the speed of the EIT system. Originally the controlling software issued these latch commands through the data acquisition card's digital controller and then triggered voltage measurements by the card. Later, integrated circuit (IC) counters were added to the EIT hardware to select injection, ground, and measurement electrodes in sequence and to trigger voltage measurements once the multiplexers were latched. In early tests with a 486 PC, the acquisition time for each 16-electrode voltage projection set was reduced from 2.7 seconds with the software command option to less than 0.75 seconds with IC counters. For this reason the software-controlled option is called "slow mode," whereas the IC-controlled option is referred to as "fast mode." Validation tests conducted using both fast and slow acquisition modes (presented later in this chapter) indicate no significant loss of accuracy with the increased acquisition speed. Presently, a Pentium PC is used to operate the system; each projection set requires 1.5 seconds in "slow mode" and less than one-half second in "fast mode."

Coaxial cable is used to carry current to and from the electrodes. To minimize current loss through the cables, voltage followers (OP42 op-amps) bring the shielding of each current-bearing cable to the same voltage as the electrode. A separate set of cables connects the electrodes to the muxes that control voltage measurements, eliminating any voltage drops from the measurements that would occur across the current-bearing cables. OP42 op-amps are also used as buffers between the electrodes and the voltage muxes.

As the measurement electrode and the ground electrode are selected by the voltage muxes, their voltage signals are passed to a Burr-Brown model PGA202 differential amplifier that measures the difference between the two voltages. The voltage on the grounded electrode is always used as the reference so that the PGA202 output represents the voltage on the measurement electrode relative to ground. The advantage of such a measurement method is that common mode noise that may be present on all the electrodes and coaxial cables is subtracted out of each measurement. The PGA202 was chosen for its good common mode rejection ratio at 50 kHz and for its programmable gain, which can allow the measurement of voltage differences over a wide dynamic range. For the experiments reported here, the gain was always set to unity, since adjustments to liquid conductivity were found to be more practical in obtaining a useful voltage range.

The signal from the differential amplifier is passed to a pair of phase-sensitive demodulators (Analog Devices model AD630). These separate the signal into two components: one in phase with the EIT carrier reference signal and the other out of phase with the carrier by 90°. One demodulator multiplies the measured electrode voltage by the carrier reference signal to obtain the carrier component, while the other uses the quadrature reference signal to obtain the out-of-phase component. By the rules of trigonometric multiplication, both demodulators produce a DC voltage superimposed on an AC voltage of 100 kHz, twice the reference frequency. These outputs are filtered using four-pole, low-pass Butterworth filters with a cutoff frequency of 25 kHz to yield only the DC components, which are proportional to the carrier and quadrature components of the measured voltages. (The recovery of both in-phase and out-of-phase signals permits the determination of the real and imaginary parts of the domain impedance, a feature that may be used in the future to distinguish between more than two phases in the domain.) The DC voltages are finally passed to the DT2839 data acquisition board, which measures the two voltages on separate analog input lines with a minimum conversion time of 2.4 μs. Two other pairs of demodulators and Butterworth filters process the voltage signal from the

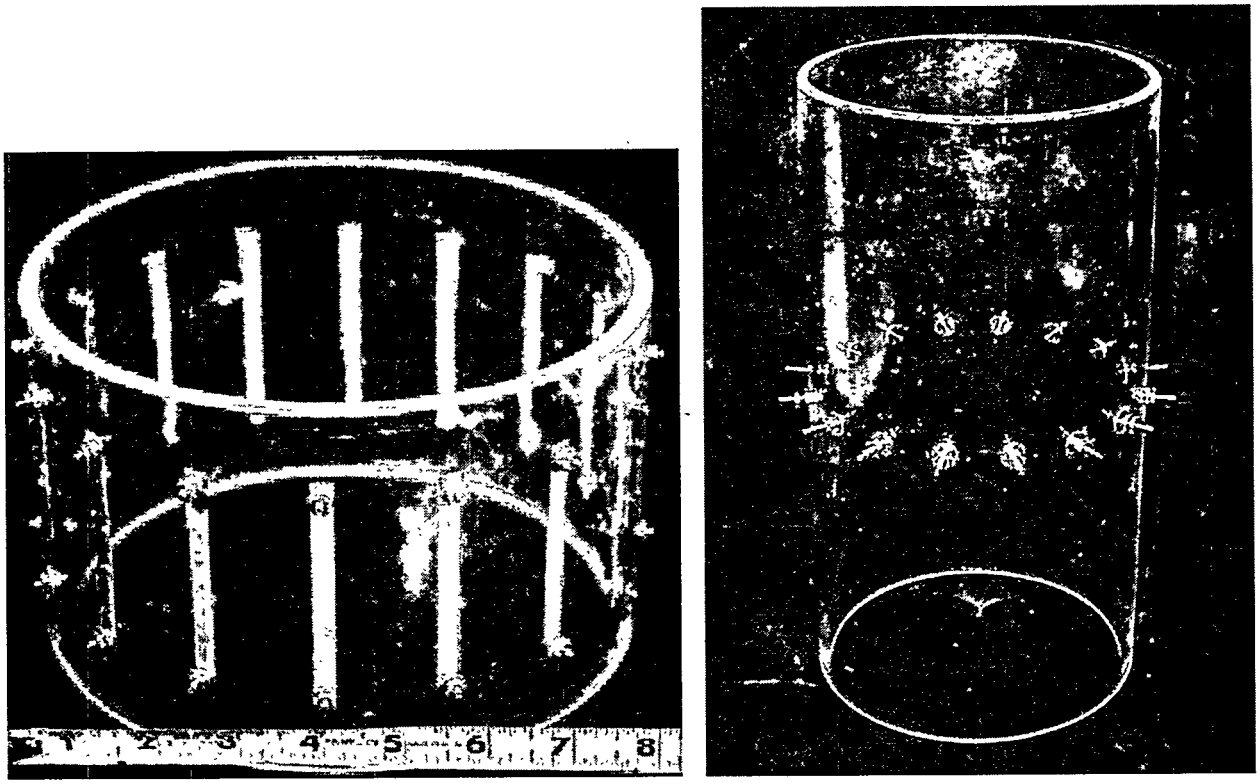

Figure 3.4. EIT electrode arrays. (Left) strip electrode array, (right) disk electrode array. Both cylinders are of the same diameter; the scale in the left-hand photo is in inches.

INA110 amplifier that monitors injection current, so that the DT2839 may measure injection current on two other input lines if necessary.

The electrode arrays used with the Sandia/Michigan system were fabricated for use as stand-alone testbeds in validation tests as well as for use in a transparent bubble column described in the next chapter. Two of these arrays are shown in Figure 3.4. Sixteen strip electrodes, each with an aspect ratio of 12, were fashioned from stainless steel strips 0.64 cm wide, 7.62 cm high, and 76 μm thick. These were mounted at equal azimuthal intervals in a Lucite cylinder with an inner diameter, D_{col}, of 19.05 cm, a wall thickness of 0.64 cm, and a height of 12.7 cm. Other electrode arrays were used during early experiments in order to evaluate the merits of different electrode geometries. Disk electrodes 1.27 cm in diameter and square electrodes 1.27 cm on a side, all 0.16 cm thick, were also fabricated from stainless steel. These were mounted at equal intervals in Lucite cylinders with the same inner diameter and wall thickness as the strip electrode cylinder but with a height of 38.1 cm, twice the inner diameter.

Each electrode geometry is known to have advantages and disadvantages. Strip electrodes can, in theory, produce relatively two-dimensional electric fields that are easier to model, provided that their length is two or more times the domain diameter. The strip electrodes do not meet this criterion, however, as is obvious from Figure 3.4. The point-like electrodes are able to produce current within a smaller domain in the axial direction than strip electrodes and are structurally more robust. However, more potential is required to inject a given amount of

current through the smaller point-like electrodes, and voids in a multiphase system may momentarily cover a disk or square injection electrode completely and severely reduce current flow into the domain. The preliminary experiments performed to evaluate these different electrode geometries are described in Section 3.4.

Two data acquisition programs on the PC are used to control the measurement electronics and data acquisition card. These codes, `FASTEIT.BAS` and `SLOWEIT.BAS`, are listed in Appendices B and C, with subroutines common to both codes listed in Appendix D. Both programs are written in Microsoft® QuickBasic™ version 4.5 (Microsoft Corporation, 1991) and call QuickBasic subroutines supplied with the SP0131 Software Toolkit (Data Translation, Inc., 1994) to drive the DT2839 and manage PC extended memory. Both codes initialize the data acquisition board and EIT electronics, initiate current injection, manipulate the collected voltage data, analyze the data for irregularities, and save the data for use by reconstruction codes. As implied by their names, `FASTEIT` arms the IC counters to quickly control the multiplexers and rotate through electrode combinations, whereas `SLOWEIT` issues the commands to the multiplexers through the digital controller on the DT2839. `FASTEIT` also allocates enough dynamic buffers in PC extended memory to collect all voltage projection sets before data manipulation, while `SLOWEIT` manipulates the data after each projection set is collected.

As implied by Eq. 3.3, the number of independent impedance parameters in the domain model increases approximately as N^2, N being the number of electrodes, but the acquisition time of the Sandia/Michigan system increases approximately as N^3. An option was installed in the software and hardware to obtain voltage projection sets using either 8 or 16 electrodes. Although a limited number of tests were performed with rings of eight electrodes, the tests were not extensive enough to justify their use in evaluating the system. This option is still available, should further study of the tradeoff between resolution and acquisition time be warranted.

3.2.2. Finite-Element Algorithm for Reconstruction of Conductivity Distributions

This subsection summarizes the reconstruction algorithm used with the Sandia/Michigan EIT system. The algorithm is based on the YWT method described by Yorkey *et al.* (1987) (see also George, 1999a). The original Sandia algorithm has been documented by Torczynski *et al.* (1997) and is shown in flowchart form in Figure 3.5. The reader is referred to that report for complete details of the original algorithm, which computed a quadratic radial conductivity profile to represent bubble-column flows. In this subsection, the recent extension of the three-dimensional algorithm to quartic profiles is discussed.

In the algorithm, the medium is surrounded by an insulating boundary through which current is injected or withdrawn at discrete electrodes. A finite-element method (FEM) representation is generated for the voltage equation governing the domain, Eq. 3.1. Unlike most finite-element methods, the conductivity is not represented by a piecewise constant function that is discontinuous at element boundaries. Instead, the electrical conductivity is represented as a global function of position and of one or more conductivity parameters. To implement the

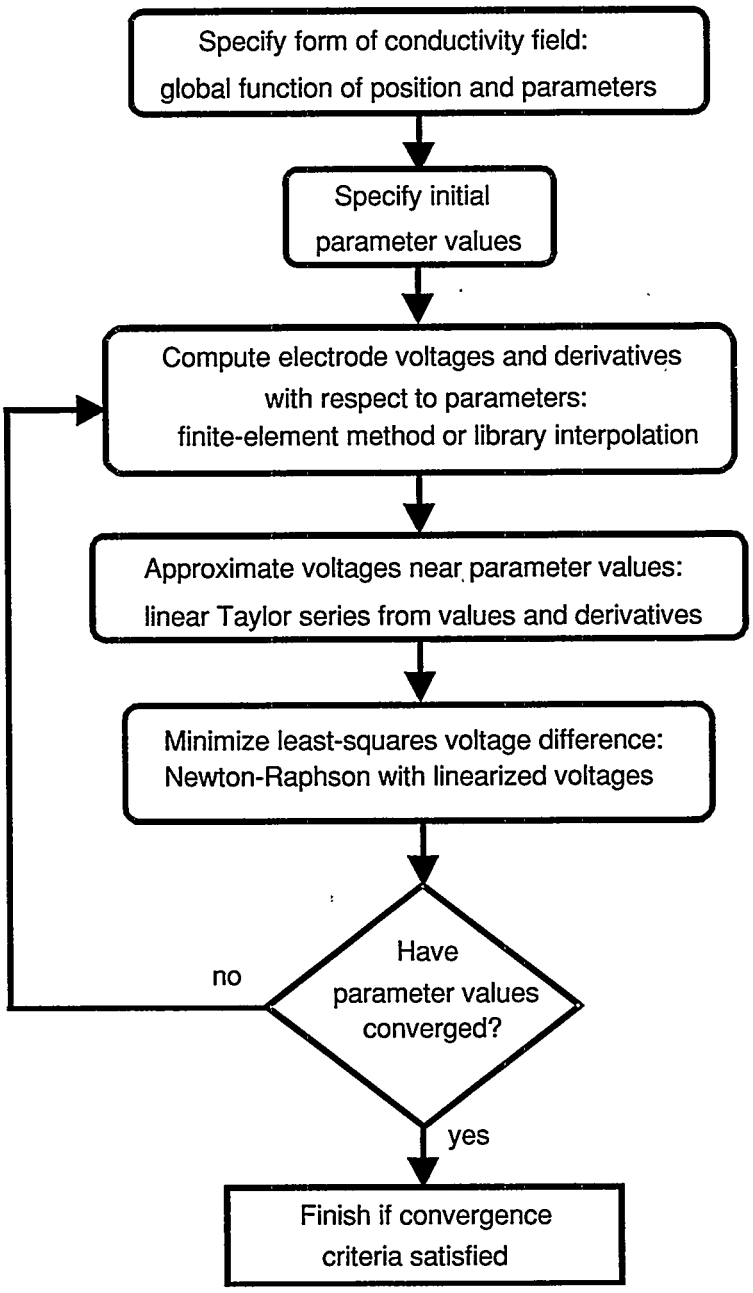

Figure 3.5. Flow chart of EIT reconstruction algorithm.

Neumann boundary conditions (Eq. 3.2), current flow is specified at the electrodes such that the net current into and out of the domain is zero.

The finite-element equations generated from Eqs. 3.1 and 3.2 are solved to find (1) the predicted voltages at the electrodes as functions of the conductivity parameters and (2) the derivatives of the electrode voltages with respect to the conductivity parameters. Subsequently, these parameters are adjusted by a Newton-Raphson algorithm to minimize the least-squares difference between the computed and experimental electrode voltages at those electrodes that do not carry current. Since no voltages are prescribed in the computational boundary conditions, the

computed voltage solution of Eq. 3.1 is unique only to within an arbitrary additive constant. The value of the additive constant is determined during the least-squares minimization process.

The algorithm is simplified by assuming that resistive effects dominate over capacitive effects in the medium. An appropriate criterion for this assumption can be obtained by separating the complex conductivity in Eq. 3.1 into its real and imaginary components (see, for example, Somersalo *et al.*, 1992):

$$\gamma = \sigma + i2\pi f\tilde{\omega}\omega_0 . \tag{3.4}$$

Here σ is the DC (or real) conductivity, $\tilde{\omega}$ is the normalized permittivity (or dielectric constant) of the medium, ω_0 is the permittivity of a vacuum (8.85×10^{-12} F/m), and f is the AC frequency. For resistance to dominate in the multiphase flows considered here, the following constraint on the liquid conductivity must be satisfied:

$$\sigma_L >> 2\pi f\tilde{\omega}_L\omega_0 . \tag{3.5}$$

For $f = 50$ kHz applied to water, for which $\tilde{\omega}_L \approx 80$, this constraint is satisfied if $\sigma_L >> 2$ μS/cm. This condition is often met by tap water and can also be attained by adding electrolytes to deionized water. In this work, controlled amounts of sodium chloride or sodium nitrate were added to deionized water to ensure that liquid conductivities were at least one hundred times this lower limit. In the remainder of this report, resistive effects are assumed to dominate over capacitive effects in all experiments and calculations, so that $\gamma \rightarrow \sigma$ in Eqs. 3.1 and 3.2.

Separate computer codes have been written to implement this algorithm in two and three dimensions. The two-dimensional code `FEMEIT`, listed in Appendix E, models arbitrary domains and represents electrodes by mesh nodes, essentially mathematical points of zero width. `FEMEIT` generates and solves the FEM equations using global conductivity functions from a subroutine library and applies the Newton-Raphson algorithm to determine the final conductivity parameters. Conductivity functions in the library include a constant conductivity, a circular insulating region at an arbitrary position, and various analytical conductivity distributions. As an example, the following formula is used for the spatial variation of conductivity, $\sigma(x,y)$, in the case of a circular insulator (Torczynski *et al.*, 1996a):

$$\sigma(x,y) = C_1\left\{1+\frac{K_1}{2}\left[\tanh\left(\frac{w-C_2}{K_2}\right)-\tanh\left(\frac{w+C_2}{K_2}\right)\right]\right\}, \tag{3.6}$$

where

$$w^2 = (x-C_3)^2 + (y-C_4)^2 . \tag{3.7}$$

This function represents a cylindrical region of normalized radius C_2, centered at $(x,y) = (C_3,C_4)$, with a boundary thickness proportional to $2K_2$. Well inside the region, the conductivity is approximately $C_1(1-K_1)$, and well outside, the conductivity is approximately

C_1. When K_1 is slightly less than unity and K_2 is slightly less than the element size, this function represents an insulating cylinder of varying position and radius. This function was used to recreate "phantom" cylinders in validation tests described later in this chapter.

The three-dimensional code EITAXI (Appendix F) models cylindrical domains within which the conductivity varies only radially but the voltage fields vary three-dimensionally due to the finite axial extent of the electrodes. As applied to multiphase flows, this code reconstructs axisymmetric and vertically uniform phase distributions without the error inherent in the unrealistic assumption that the electric field lines are similarly limited to two-dimensionality. The electrodes around the cylindrical domain are taken to be identical and positioned at equal azimuthal intervals. Unlike FEMEIT, EITAXI represents each electrode with its actual shape rather than as a mathematical point. The conductivity field is represented as a global function of radial position and of conductivity parameters. Rather than solving the three-dimensional finite-element representation of the voltage field directly, as FEMEIT does in the two-dimensional case, EITAXI uses library files that contain the fundamental electrode voltages at discrete values of the conductivity parameters (Torczynski *et al.*, 1996a, 1997). These library files are computed in advance using the commercial finite-element code FIDAP (Fluid Dynamics International, 1996), as demonstrated later in this subsection. A cubic-spline interpolation is used to determine the fundamental electrode voltages for intermediate values of the conductivity parameters. To find the parameter values that best describe the experimental conductivity distribution, the least-squares difference between the experimental voltages and appropriate linear combinations of the computed voltages is determined. A Newton-Raphson algorithm is then used to determine the values of the conductivity parameters that minimize this least-squares difference.

As part of the axisymmetric reconstruction process, FIDAP generates a set of nondimensional, fundamental voltage solutions, $\{V_0 \ldots V_{N/2}\}$, for the parameter libraries used by EITAXI in evaluating experimental data (Torczynski *et al.*, 1997). The supplementary computer code EITFUN (described and listed in Appendix G) was written to compute fundamental voltage solutions from axisymmetric experimental datasets, the reverse of the usual process. Comparisons of the computational and experimental fundamental solutions for no-flow conditions allowed different electrode geometries to be evaluated, as described at the end of this chapter. Another code listed in Appendix H, EITFUL, uses fundamental voltage solutions to build axisymmetric datasets that can be used to validate the reconstruction algorithms.

The simplification of the conductivity field in EITAXI to allow only radial variations is justified by the fact that all experiments are conducted in cylindrical domains, and azimuthally invariant phase distributions are reasonably expected for the conditions studied in this work. Various conductivity distributions employed to date in EITAXI include a uniform conductivity profile; symmetric second-order (quadratic) and fourth-order (quartic) polynomials in the radius, r; and a cylindrical insulating inclusion centered in the domain. Originally a quadratic radial conductivity profile was used to represent bubble-column flows in all EIT reconstructions. However, results from the combination of EIT and gamma-densitometry tomography (GDT) in early three-phase experiments (George *et al.*, 1999a; see also Chapters 4 and 5) suggested that a quartic profile would be necessary. The lack of a quartic term in the EIT algorithm and the presence of one in the GDT algorithm were proposed as an explanation for slight on-axis maxima in reconstructed solid volume fraction profiles. To evaluate this proposal and to make

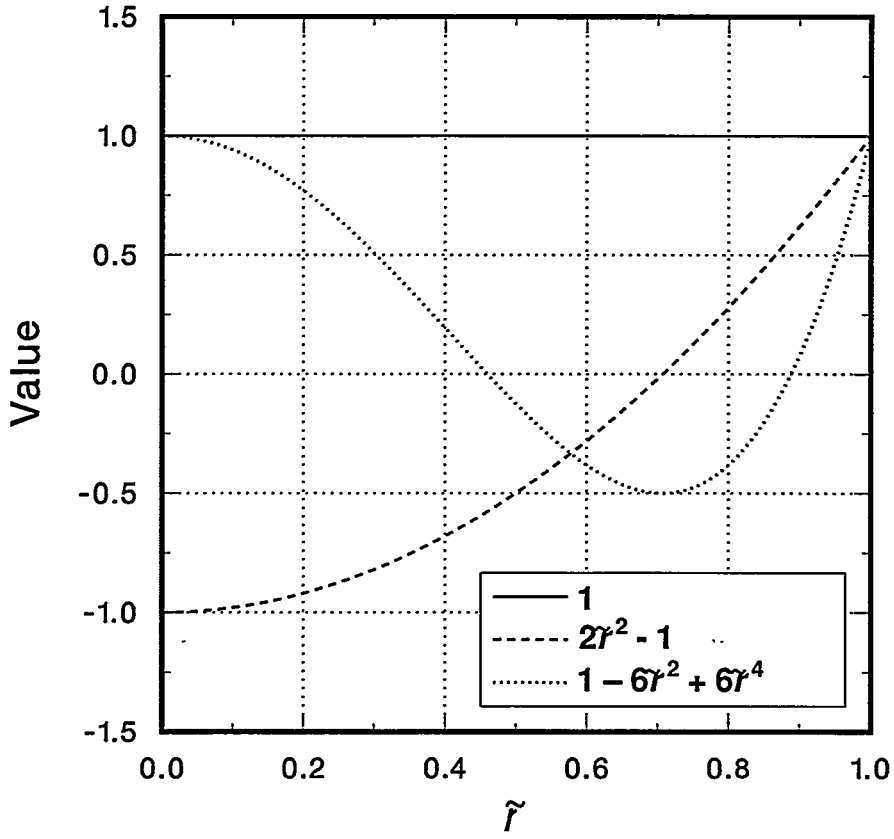

Figure 3.6. Basis functions used in EIT quartic algorithm.

EIT and GDT equally general, the EIT algorithm described by Torczynski *et al.* (1997) was extended to include a quartic term. The remainder of this subsection describes the quartic model and its development.

The following representation of a quartic radial conductivity profile was chosen:

$$\frac{\sigma(r)}{\sigma_L} = \frac{1 + C_1\left(2\tilde{r}^2 - 1\right) + C_2\left(1 - 6\tilde{r}^2 + 6\tilde{r}^4\right)}{C_0}, \tag{3.8}$$

where C_1 and C_2 are the conductivity shape parameters, C_0 is a scale parameter, $\tilde{r} = r / R_{col}$, r is the radial coordinate, and R_{col} is the radius of the circular domain – *e.g.*, the testbed or bubble column. The basis functions (the functions of $\tilde{r}$ in parentheses) were chosen so that the average of the product of any two different basis functions over the cross-sectional area of the domain vanishes,

$$\int_0^1 1\left(2\tilde{r}^2 - 1\right)2\tilde{r}\,d\tilde{r} = \int_0^1 1\left(1 - 6\tilde{r}^2 + 6\tilde{r}^4\right)2\tilde{r}\,d\tilde{r} = \int_0^1 \left(2\tilde{r}^2 - 1\right)\left(1 - 6\tilde{r}^2 + 6\tilde{r}^4\right)2\tilde{r}\,d\tilde{r} = 0, \tag{3.9}$$

and so that the values of the basis functions at $\tilde{r} = 1$ are 1. Figure 3.6 shows a plot of these three basis functions.

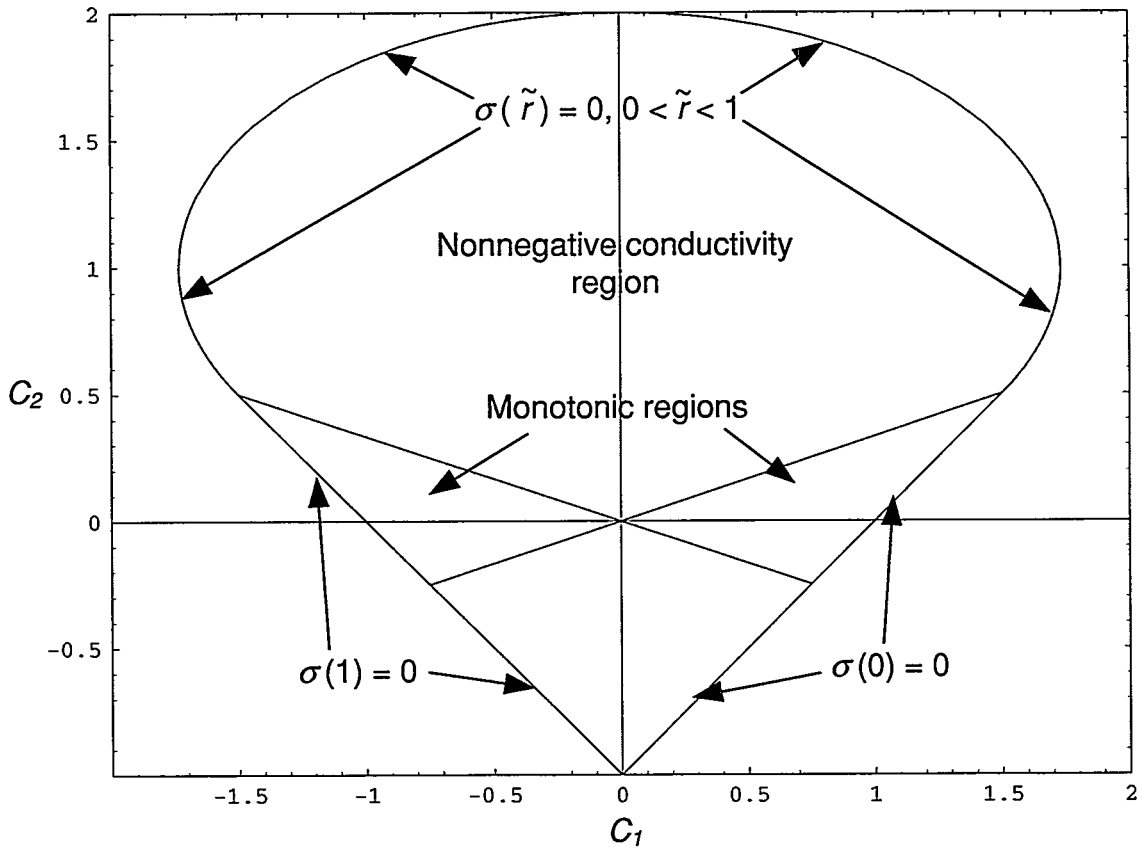

Figure 3.7. Region of parameter space in which conductivity is nonnegative at all radial locations.

The coefficients C_1 and C_2 that multiply the quadratic and quartic basis functions describe a two-dimensional parameter space. The condition that the conductivity must remain nonnegative for all radial locations constrains the coefficients to lie only within a portion of this parameter space. The boundary of the physically allowable portion of this two-dimensional space, within which the conductivity is nonnegative at all radial locations, is governed by the following equations, as shown in Figure 3.7:

$$|C_1| \le C_2 + 1 \text{ when } -1 \le C_2 \le \frac{1}{2}, \tag{3.10a}$$

$$|C_1| \le \left\{3\left[1-(1-C_2)^2\right]\right\}^{1/2} \text{ when } \frac{1}{2} \le C_2 \le 2. \tag{3.10b}$$

Monotonic conductivity profiles obey the following additional constraint, also shown in Figure 3.7.

$$|C_2| \le |C_1|/3 \tag{3.11}$$

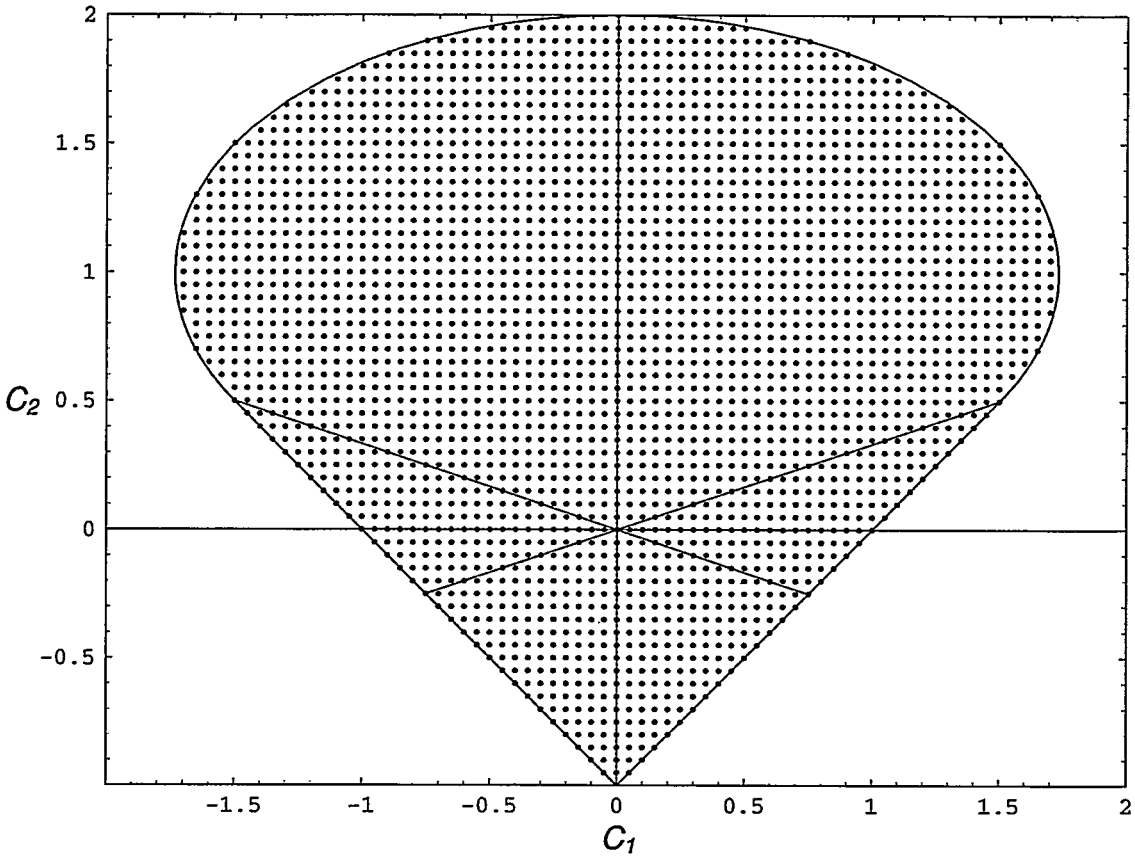

Figure 3.8. Discrete points in parameter space at which FIDAP computations were performed (2675 total).

The fundamental voltage solutions were computed for values of C_1 and C_2 within these constraints. Figure 3.8 shows the discrete points in the two-dimensional parameter space at which the fundamental voltage solutions were computed. A uniform spacing of 0.05 in both coordinate directions was employed, yielding 2675 points within the physically allowable region of parameter space. FIDAP was again used to produce the fundamental voltage solutions at the prescribed points. The FIDAP command language (Fluid Dynamics International, 1996) was employed to execute FIDAP computations in sequence and automatically loop over all the prescribed points in parameter space; approximately 80 hours on a Sun workstation was required to complete these calculations. The EIT electrode geometry used by FIDAP and `EITAXI` corresponds to the strip electrode ring shown in Figure 3.4. The mesh used in the computations, shown in Figure 3.9, has two symmetry planes and terminates at a height of two diameters. This mesh was previously found to produce acceptable accuracy (Torczynski *et al.*, 1998), although the accuracy degrades somewhat as the boundary of parameter space is approached – *i.e.*, when the conductivity vanishes at some radial coordinate within the computational domain.

With the fundamental voltage solutions computed for all points within the parameter space, the final step was to create smooth functions representing the solutions at all points within the physically meaningful region of parameter space, rather than just at the discrete points at which computations were made. Smooth functions are needed because the Newton-Raphson

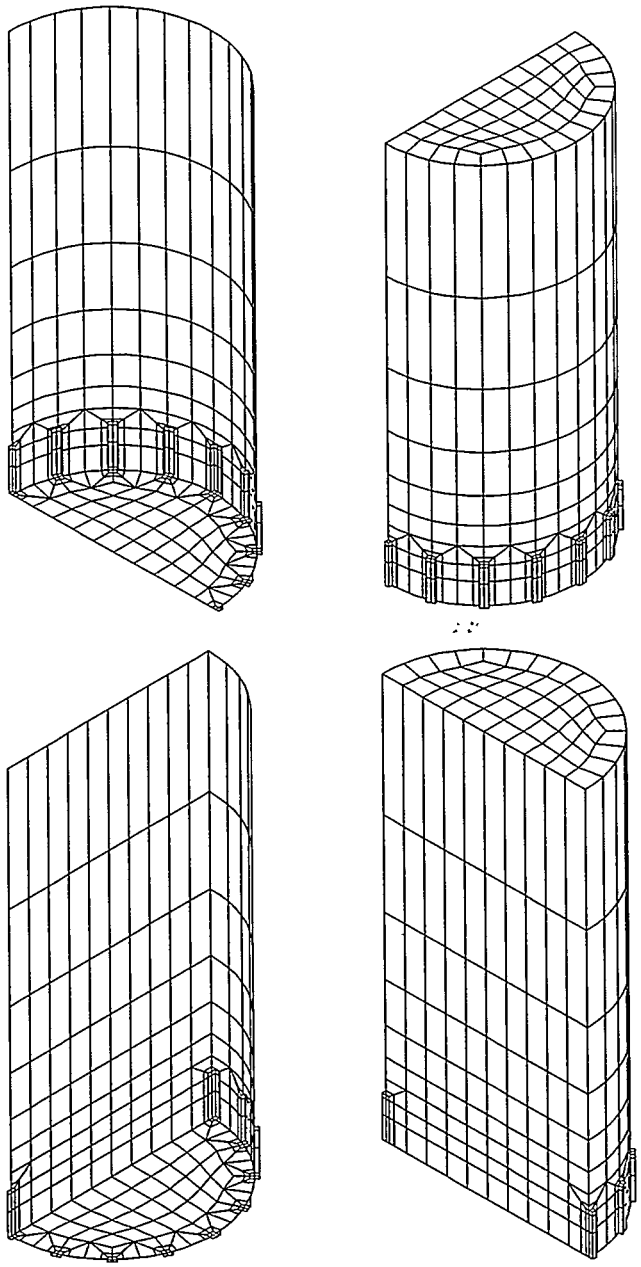

Figure 3.9. FIDAP mesh on which fundamental voltage solutions were computed.

method described earlier requires continuous, well-behaved first derivatives of the fundamental voltage solutions with respect to the conductivity parameters. Because the conductivity vanishes at some location within the physical domain for parameter values lying on the parameter-space boundary, the fundamental voltage solutions experience rapid changes as this boundary is approached. The point $(C_1, C_2) = (-1.5, 0.5)$ is a particularly strong singularity, since both the conductivity and its radial derivative $\partial\sigma/\partial r$ vanish at $\tilde{r} = 1$ for these particular values. The large voltage values encountered near the boundary and the rapid variation in voltage values as this boundary is approached render polynomial fits inaccurate; however, polynomial fits to the

reciprocals of the values of the fundamental voltage solutions are well behaved as the boundary is approached.

The symbol manipulation code Mathematica (Wolfram, 1996) was used to fit polynomials of degree 24 in both C_1 and C_2 (containing a total of 625 fitting coefficients k) to the reciprocal nontrivial voltages of the fundamental solutions, with derivatives determined by the chain rule:

$$\frac{1}{V_n} \rightarrow \sum_{i=0}^{24}\sum_{j=0}^{24} k_{nij} C_1^i C_2^j, \; n = 1\text{K } N/2. \tag{3.12}$$

Note that by definition the ground electrode voltage $V_0 = 0$ and is not included in the fits. Of the 2675 points in (C_1, C_2) parameter space, 2670 are used in the fits: the other five points are too close to the parameter-space boundary to be computed accurately on the mesh shown in Figure 3.9 and corrupt the fit if included. For comparison, the computed values and the polynomial fit for voltage V_7 along the curves $C_1 = 0$ and $C_2 = 0$ are shown in Figure 3.10, and are seen to agree closely.

3.2.3. Determination of Volume Fraction Distributions from Conductivity Distributions

Once the converged parameters from `FEMEIT` or `EITAXI` have been used to construct a conductivity distribution, a constitutive model is required to relate the electrical conductivity to the conducting and insulating phase volume fractions. When the continuous liquid phase is the only conducting phase, the Maxwell-Hewitt relation (Maxwell, 1881; Hewitt, 1978) can be used to relate $\sigma(r)$, the local mixture conductivity, and σ_L, the known liquid conductivity, to the local liquid volume fraction $\varepsilon_L(r)$:

$$1-\varepsilon_L(r) = \frac{1-[\sigma(r)/\sigma_L]}{1+\frac{1}{2}[\sigma(r)/\sigma_L]} \text{ (three-dimensional inclusions).} \tag{3.13}$$

The expression above assumes three-dimensional inclusions of an insulating phase dispersed in the conducting phase, such as gas bubbles or insulating solid particles dispersed in salt water, and is applied locally in all tomographic reconstructions in this report. An analogous relation can be derived for the somewhat artificial case of two-dimensional insulating inclusions dispersed in a conducting phase (*e.g.*, parallel insulating posts in salt water):

$$1-\varepsilon_L(r) = \frac{1-[\sigma(r)/\sigma_L]}{1+[\sigma(r)/\sigma_L]} \text{ (two-dimensional inclusions).} \tag{3.14}$$

Equation 3.14 is not used in any of the tomographic reconstructions in this study, but is used to assess the amount of uncertainty introduced into the reconstructions by the Maxwell-Hewitt constitutive model.

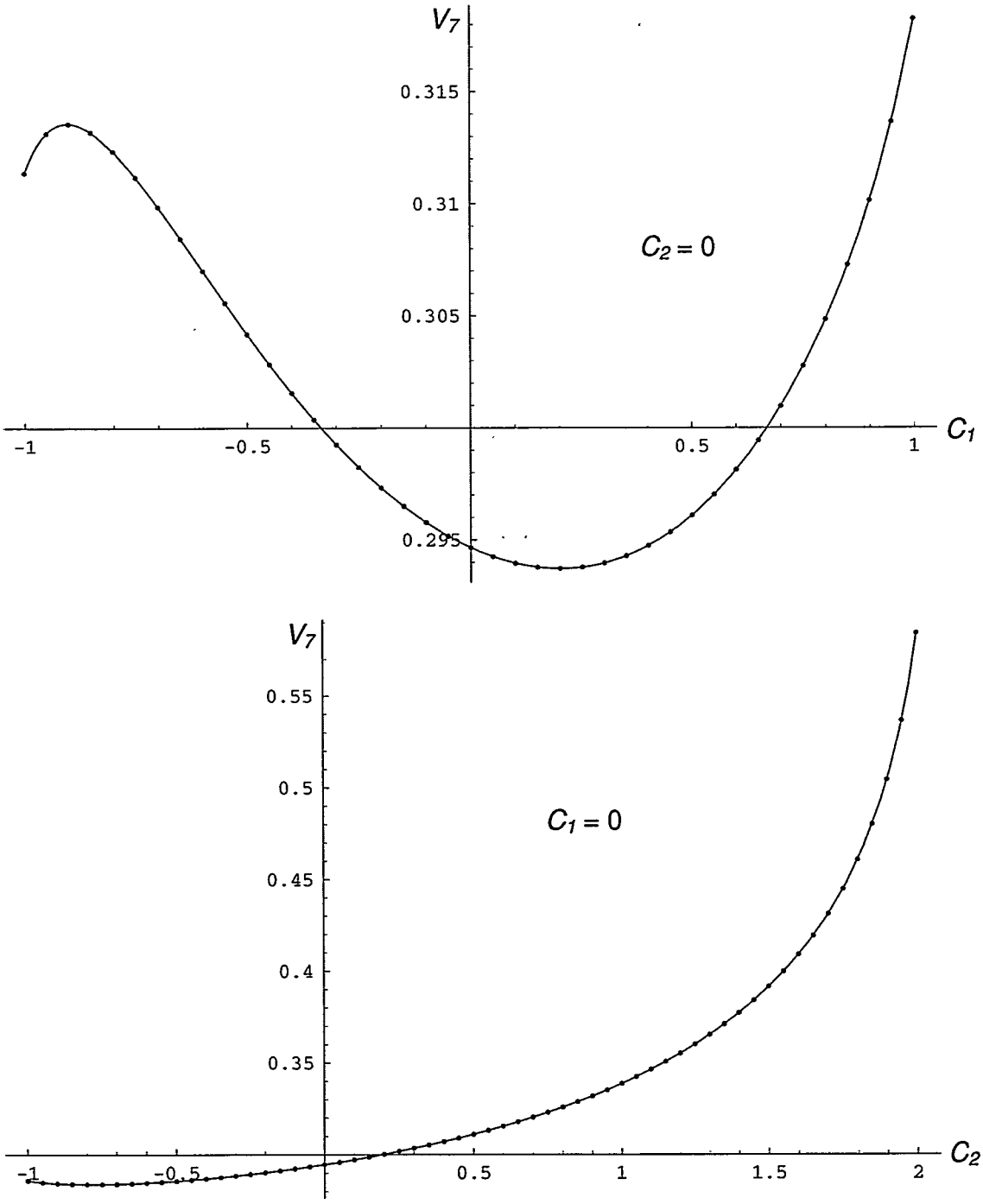

Figure 3.10. Plots of fundamental voltage V_7 along selected curves. Points are computed with FIDAP, curves are best fits.

By continuity, the quantity $1-\varepsilon_L(r)$ equals the local insulating phase volume fraction in either geometry. To determine the domain-averaged phase volume fractions, the profiles can be analytically integrated over the domain. The values of σ_L used to obtain phase volume fractions in all experiments were determined with the EIT system itself, using measurements of the

domain with only liquid present. A good measurement of liquid conductivity is crucial for obtaining quantitative data and requires careful control of test conditions, since conductivity can vary significantly with temperature and the presence of contaminants in the liquid.

3.3. Validation of Reconstruction Algorithms

The algorithms described above for reconstructing conductivity profiles have been validated using both analytically and physically derived projection sets. The physical data were obtained during tests of the complete EIT system with the detection of a series of insulating inclusions in the test domain. The constitutive relationship used to translate conductivity profiles into phase volume fraction profiles was also investigated for accuracy, and the sensitivity of reconstructions to noise in the measured voltages was determined. This section describes these tests and presents the results.

3.3.1. Numerical Validation of Conductivity Reconstruction Algorithm

Several calculations were performed to validate the conductivity reconstruction algorithm. The two tests described in this section were first documented in Torczynski *et al.* (1997) but are repeated here for completeness. The first test involved an analytical result for the two-dimensional voltage distribution $V(x, y)$ in a circular domain of constant conductivity σ. The boundary conditions were defined by a current per unit electrode length, J, injected at the boundary point (x_o, y_o) and withdrawn at the boundary point $(x_o, -y_o)$; this yielded the analytical result

$$V(x,y) = (J/2\pi\sigma)\ln\left[\frac{(y_o+y)^2+(x_o-x)^2}{(y_o-y)^2+(x_o-x)^2}\right]. \tag{3.15}$$

The uniform domain was bounded by 16 electrodes located at equal intervals of 22.5º around the perimeter. The radius of the circular domain, the current per unit length and the constant conductivity were all set to unity.

By rotating the coordinates of the analytical results derived from selected injection and withdrawal combinations, the boundary voltages for all possible injection and withdrawal pairs were determined from the analytical solutions. These analytical voltages were input to `FEMEIT`, along with mesh information, to find the effect of mesh size on reconstruction accuracy. The conductivity function was chosen to be a single unknown constant throughout the domain. Table 3.1 shows the dependence of the constant conductivity determined by `FEMEIT` for five meshes of appreciably different nodal density. An ideal result would be a calculated conductivity of unity. In all cases the calculated result is close to unity, and is converging to unity with increasing nodal density (Torczynski *et al.*, 1996a).

Table 3.1. Effect of FEMEIT mesh refinement on reconstruction accuracy of a uniform domain. The correct analytical solution is $\sigma = 1$.

Mesh	Number of nodes	Number of elements	Computed σ
A	25	32	1.0443
B	81	128	1.0122
C	169	288	1.0047
D	289	512	1.0023
E	441	800	1.0013

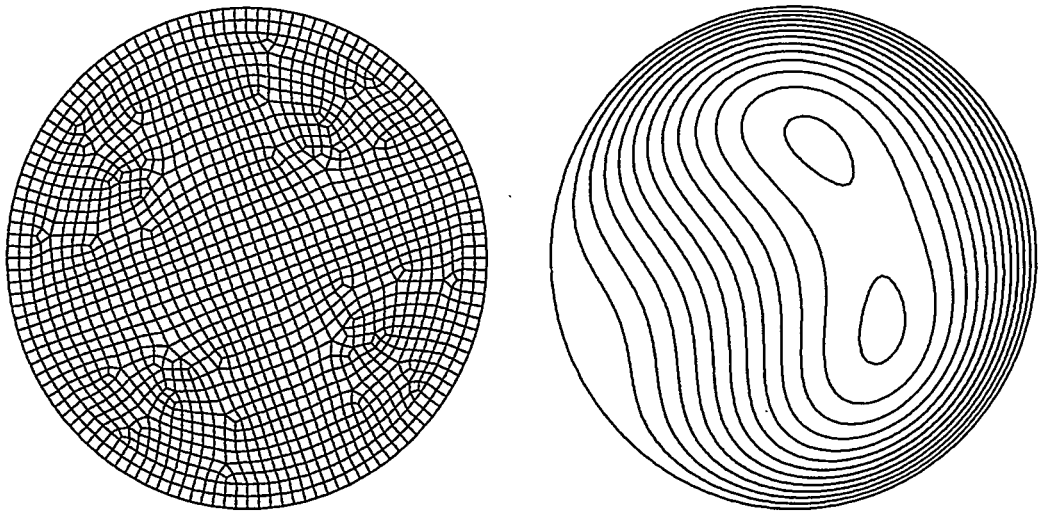

Figure 3.11. Finite-element mesh used by FIDAP in validation tests (left) and synthetic benchmark conductivity field (right). Adapted from Torczynski *et al.* (1996a).

In the second set of validation calculations, the finite-element code FIDAP was used to compute the boundary voltages corresponding to the synthetic spatial conductivity distribution shown in Figure 3.11. This distribution mimics a bubble-column flow with an excess of bubbles in the upper right quadrant. The electrode geometry was identical to that used in the first problem, but a highly refined mesh was used to guarantee that the FIDAP solution would be mesh-independent. The computed voltages from FIDAP were input to FEMEIT to test its ability to reproduce the original conductivity distribution, and reconstructions were performed using the same five meshes used in the first calculation set (Table 3.1).

Figure 3.12 shows the most refined mesh used for this simulation (mesh E of Table 3.1) and the reconstructed conductivity field produced by the EIT algorithm for this mesh. Agreement is seen to be good. To quantify the effect of mesh refinement on reconstruction accuracy, average and rms conductivity values were computed for the FEMEIT results on each mesh and are listed in Table 3.2. As the mesh is refined, the average conductivity approaches the analytical average value of 2/3, and the rms value tends to zero.

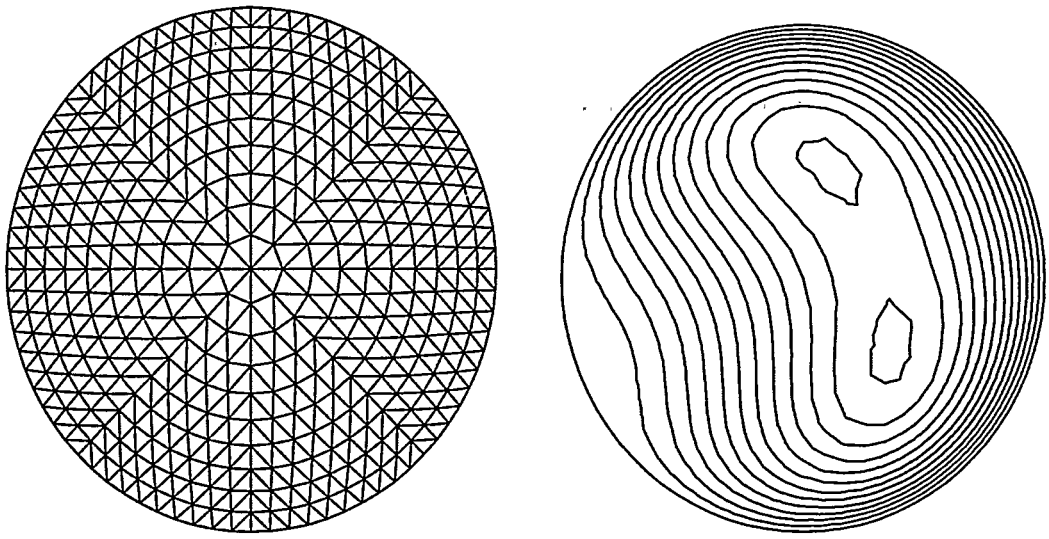

Figure 3.12. Finite-element mesh used by FEMEIT in validation tests (left) and reconstructed conductivity field (right). Adapted from Torczynski *et al.* (1996a).

Table 3.2. Effect of FEMEIT mesh refinement on reconstruction accuracy of a synthetic conductivity distribution. The analytical average of the synthetic distribution is $\sigma = 2/3$.

Mesh	Computed σ	rms deviation in σ
A	0.679	0.170
B	0.676	0.027
C	0.669	0.007
D	0.666	0.003
E	0.666	0.003

3.3.2. Experimental Validation of Reconstructed Conductivity Profiles

The reconstruction algorithm was also validated using experimental data from both the strip and point-like electrode arrays. Validation experiments with the strip electrodes were performed by capping the bottom of the cylinder containing the electrode array (Figure 3.4) to form a static testbed, filling the testbed with a saltwater solution of known conductivity, and placing smaller Lucite cylinders of known diameter in the testbed to act as insulating inclusions. EIT voltage measurements were then taken of the domain and used to reconstruct the location and position of the insulating "phantom." This type of test has been studied extensively by other investigators of EIT (*e.g.*, Duraiswami *et al.*, 1997), and was performed with the original configuration of the Sandia/Michigan EIT system as well (Torczynski *et al.*, 1997).

To limit the test domain in the vertical direction, the free surface of the liquid and the bottom Lexan end cap were aligned with the top and bottom ends of the strip electrodes, respectively. This eliminated axial electric field variations and enforced two-dimensionality.

Table 3.3. Comparison of actual and reconstructed geometries of insulating inclusions in two-dimensional validation tests with strip electrodes.

Actual conditions			PC electrode selection (SLOWEIT)			IC electrode selection (FASTEIT)		
$D_{cyl}/2R_{col}$	r/R_{col}	$\bar{\varepsilon}_{cyl}$	$D_{cyl}/2R_{col}$	r/R_{col}	$\bar{\varepsilon}_{cyl}$	$D_{cyl}/2R_{col}$	r/R_{col}	$\bar{\varepsilon}_{cyl}$
0	–	0	0.062	0.000	0.004	0.059	0.000	0.004
0.266	0.596	0.071	0.271	0.597	0.074	0.271	0.597	0.074
0.300	0.000	0.090	0.309	0.020	0.095	0.308	0.020	0.095
0.534	0.189	0.285	0.530	0.184	0.281	0.530	0.184	0.280

Cylinders of different diameters were placed both eccentrically and concentrically with the vertical axis of the testbed to mimic different distributions of gas in a bubble column. Data were acquired using both the PC software (SLOWEIT) and IC counters (FASTEIT) to select electrode combinations.

The conducting medium was deionized water with sodium chloride solution added to yield a conductivity of $\sigma_L = 420 \pm 5$ μS/cm for all strip electrode validation cases. Experience with the EIT system has shown that the conductivity of the continuous phase must be chosen carefully for each geometry and multiphase system to obtain good resolution in the voltage measurements. Because the EIT system employs a constant injection current, a conductivity that is too high will lower the voltages across the domain to the point of poor resolution, while a conductivity that is too low will produce voltages beyond the input range of the data acquisition board. The conductivities used in these and all other tests were selected to provide a large dynamic range of measured voltages without exceeding the input limit of the DT2839.

Equations 3.6 and 3.7 were employed as the spatial conductivity function in the FEMEIT reconstructions. Values of $K_1 = 0.99$ and $K_2 = 0.03$ were used, and the resulting reconstructions were found to be insensitive to modest changes from these values. Table 3.3 presents, for each test case, the actual diameter D_{cyl} of the test object and the radial offset distance r of the object center from the testbed central axis, both normalized by the domain radius, R_{col}. The table also presents the normalized computed diameter, $D_{cyl}/2R_{col} = C_2$, and the offset distance, $r/R_{col} = \sqrt{C_3^2 + C_4^2}$, determined from the EIT data. A domain-averaged inclusion volume fraction, $\bar{\varepsilon}_{cyl} = (D_{cyl}/2R_{col})^2$, was also computed from the actual and reconstructed object dimensions. Figure 3.13 shows the reconstructed conductivity distributions for two of the four test cases; the light areas indicate the object boundaries, numerical transition regions from high conductivity outside the object to zero conductivity within the object.

The reconstructions are in good agreement with actual conditions, reproducing the volume fraction to within 0.005 in $\bar{\varepsilon}_{cyl}$ and the distance r of the inclusion from the central axis to within 3%. For the smaller inclusions the diameter of the object (and hence the average volume fraction) was always slightly overpredicted; in the case of the largest test object, the volume fraction was underpredicted. The source of the disagreement is believed to be differences

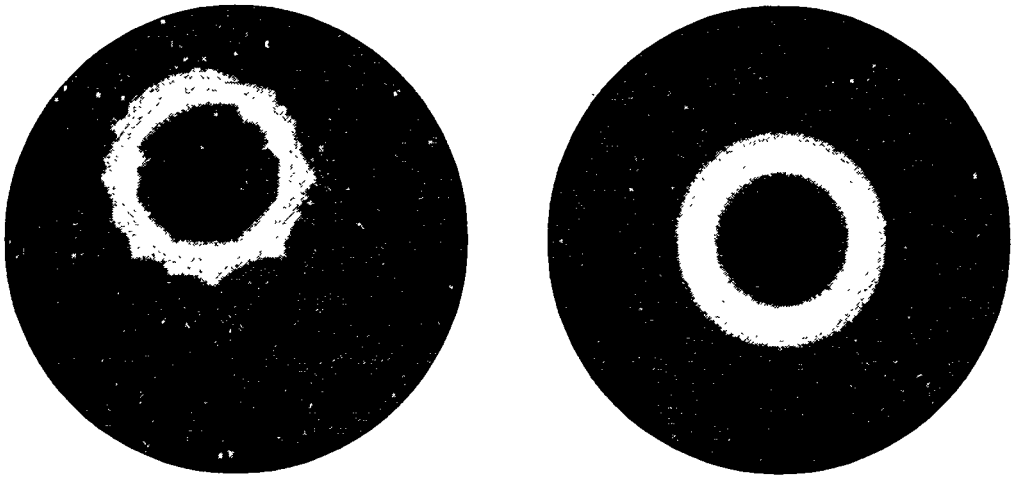

Figure 3.13. Conductivity reconstructions for two-dimensional validation tests with inclusions. (Left) $D_{cyl} = 5.07$ cm, $r = 5.68$ cm; (right) $D_{cyl} = 5.72$ cm, $r = 0$.

Table 3.4. Fundamental voltage solutions for 16 strip electrodes in the transparent bubble column.

Fundamental voltage	Computational value	Experimental value
V_0 (reference)	0	0
V_1	0.002275	0.002295
V_2	0.009430	0.009481
V_3	0.02260	0.02252
V_4	0.04432	0.04392
V_5	0.08030	0.07963
V_6	0.1454	0.1443
V_7	0.2947	0.2930
V_8 (current-bearing)	1.327	1.232

between the measured and reconstructed voltages along the domain boundary. An example of these differences can be found by comparing the computed and experimental fundamental voltages $\{V_1 \ldots V_7\}$ in Table 3.4. While the computed voltages match the corrected experimental data to within 1% at each non-current-bearing electrode, changes in the sign and magnitude of the difference indicate slightly different "shapes" of the computed and experimental voltage profiles along the boundary. This would produce slight differences between the actual and reconstructed conductivity profiles.

Notably, the reconstruction algorithm produced a small object when none was present. This indicates that objects of diameters $D_{cyl}/2R_{col} \leq 0.06$ cannot be reconstructed and that the uncertainty in $\bar{\varepsilon}_{cyl}$ is on the order of 0.004. This uncertainty is attributed to slight differences

Table 3.5. Comparison of actual and reconstructed geometries of insulating inclusions in three-dimensional validation tests with disk electrodes.

Actual conditions		PC electrode selection (SLOWEIT)		IC electrode selection (FASTEIT)	
$D_{cyl}/2R_{col}$	$\bar{\varepsilon}_{cyl}$	$D_{cyl}/2R_{col}$	$\bar{\varepsilon}_{cyl}$	$D_{cyl}/2R_{col}$	$\bar{\varepsilon}_{cyl}$
0	0	0.072	0.005	0.028	0.001
0.266	0.071	0.277	0.077	0.270	0.073
0.530	0.281	0.530	0.281	0.530	0.281

between the computational and experimental boundary voltages for a uniform conductivity field, similar to those for nonuniform fields discussed above.

Validation tests were also conducted with the disk and square electrodes (George *et al.*, 1998b). In these tests, a cylindrical testbed was created by placing the electrode cylinder between two more Lucite sections of the same diameter and wall thickness but 19.05 cm high. This created a test vessel with a height-to-diameter ratio of 4, tall enough to encompass the significant electric field lines. Test cases were created with tall Lucite cylindrical "phantoms" which extended along the entire height of the testbed. Because the three-dimensional reconstruction code `EITAXI` does not contain a library conductivity function for an eccentrically placed inclusion, all "phantoms" were centered on the vertical axis of the testbed. The conductivity in these tests was $\sigma_L = 604 \pm 2$ μS/cm, higher than the value in the strip electrode tests because of the smaller electrode area available for current injection.

Data were again taken using both the PC software and IC counters to select electrode combinations. Table 3.5 presents, for each test, the normalized diameter of the test object, the normalized diameter determined from the voltage data, and the domain-averaged volume fraction computed from the reconstructed diameter. The reconstructions in the table are again in good agreement with actual conditions, reproducing the volume fraction to within 0.006 in $\bar{\varepsilon}_{cyl}$. The same overprediction of smaller inclusions is seen here as was observed with the strip electrodes, but the larger inclusion is reproduced correctly.

3.3.3. Validation of Maxwell-Hewitt Relations

To assess the accuracy of the Maxwell-Hewitt relations (Eqs. 3.13 and 3.14), the computational fluid dynamics code FIDAP was used to perform simulations of the voltage field in various multiply periodic geometries. Two-dimensional square lattices of insulating squares and circles and three-dimensional simple-cubic lattices of cubes and spheres were examined; the region outside the insulating inclusions was filled with a uniformly conducting medium. Because of the symmetry and periodicity of these geometries, the computational domain consisted of only one quadrant of a two-dimensional unit cell or one octant of a three-dimensional unit cell. In each case the computational domain had a side length of unity and a conductivity of unity outside the insulating inclusion. Voltages of zero and unity were applied on two opposing sides of the domain, and insulating conditions were applied on the remaining

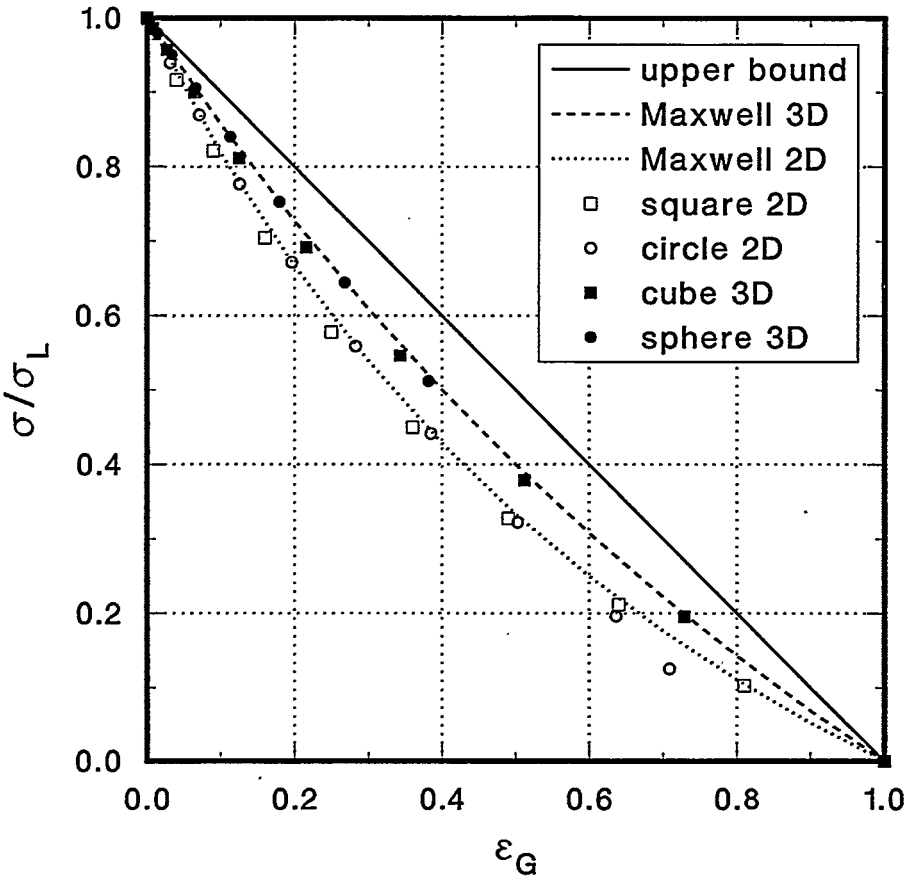

Figure 3.14. Comparison of effective conductivities computed by FIDAP with predictions from the Maxwell-Hewitt relations.

sides by virtue of symmetry. In the absence of an insulating inclusion – *i.e.*, when the domain is simply a conducting square or cube – these conditions lead to a current of unity passing through the domain along one of its principal directions. When an inclusion is present, the current is reduced from this value by the ratio of the effective conductivity to the actual conductivity, $\overline{\sigma}/\sigma_L$ (per Ohm's Law).

Figure 3.14 compares these effective conductivity ratios with the values predicted by the Maxwell-Hewitt relations for two-dimensional and three-dimensional insulating inclusions. The symbols represent FIDAP results, which are the exact solutions for converting conductivity measurements to insulating volume fractions. The dashed lines are values predicted by Eqs. 3.13 and 3.14. The upper bound, determined by the limiting case where current travels through a single layer of liquid and a single layer of gas arranged in "parallel," is plotted as the solid line. It can be seen that using the Maxwell-Hewitt relations for insulating objects of these shapes will cause the insulating phase volume fraction to be only slightly overestimated. The results for circles and spheres closely follow the Maxwell-Hewitt relations until the inclusions touch. It is concluded that these relations are of uniformly good accuracy so long as inclusions are not highly distorted and can "fill space without overlapping."

The Maxwell-Hewitt relation has been shown to be reasonably accurate for monodisperse bubble-size distributions. However, in churn-turbulent bubble-column flow there may be a bimodal distribution of bubble sizes, with many small bubbles and some large bubbles. It is important to quantify the errors that result from applying the monodisperse Maxwell-Hewitt relation to this situation. To this end, a bimodal distribution of bubbles is examined for which the ratio of bubble diameters is large compared to unity. The Maxwell-Hewitt relation is used recursively in this analysis to determine the effective conductivity of this medium.

Consider a mixture of a liquid of conductivity σ_L and an insulating gas. The gas has a total volume fraction of ε_G, and is distributed in the form of "large" bubbles that have a volume fraction of $f_{\text{large}}\varepsilon_G$ and "small" bubbles that have a volume fraction of $(1-f_{\text{large}})\varepsilon_G$. The large-bubble fraction, f_{large}, obeys the constraint $0 \le f_{\text{large}} \le 1$. The Maxwell-Hewitt relation can be applied recursively to determine the effective conductivity of this medium. In a model similar to that of Krishna and Ellenberger (1996) in Section 2.3.1, the liquid and the small bubbles form a "dense phase" mixture with an effective conductivity σ_{df} given by

$$\frac{\sigma_{df}}{\sigma_L} = \frac{1-\varepsilon_{df}}{1+\frac{1}{2}\varepsilon_{df}}, \tag{3.16}$$

where (compare to Eq. 2.26)

$$\varepsilon_{df} = \frac{(1-f_{\text{large}})\varepsilon_G}{1-f_{\text{large}}\varepsilon_G} = \frac{\varepsilon_{G,small}}{1-\varepsilon_{G,large}}. \tag{3.17}$$

The large bubbles and the "dense phase" form another mixture, denoted B (bimodal), with an effective conductivity σ_B given by

$$\frac{\sigma_B}{\sigma_{df}} = \frac{1-\varepsilon_{G,large}}{1+\frac{1}{2}\varepsilon_{G,large}}, \tag{3.18}$$

where

$$\varepsilon_{G,large} = f_{\text{large}}\varepsilon_G. \tag{3.19}$$

These relations can be combined to determine the effective conductivity of the bimodal bubble mixture in terms of the total gas volume fraction and the fraction f_{large} of the gas in large bubbles, the bimodal Maxwell-Hewitt relation:

$$\frac{\sigma_B}{\sigma_L} = \left[\frac{1-f_{\text{large}}\varepsilon_G}{1+\frac{1}{2}f_{\text{large}}\varepsilon_G}\right]\left[\frac{1-\varepsilon_G}{1-\frac{3}{2}f_{\text{large}}\varepsilon_G+\frac{1}{2}\varepsilon_G}\right]. \tag{3.20}$$

When $f_{large} = 0$ or $f_{large} = 1$, this expression reduces to the monodisperse Maxwell-Hewitt relation, essentially Eq. 3.13:

$$\frac{\sigma}{\sigma_L} = \frac{1-\varepsilon_G}{1+\frac{1}{2}\varepsilon_G}. \tag{3.21}$$

For any value of f_{large} between 0 and 1, the bimodal curve lies slightly beneath the monodisperse curve. Thus, the assumption of a monodisperse bubble-size distribution in the presence of a bimodal bubble-size distribution would cause the gas volume fraction to be slightly overpredicted. The large-bubble fraction at which the maximum difference between the monodisperse and bimodal Maxwell-Hewitt relations occurs for a given total gas volume fraction is then

$$f_{max} = \frac{1-\sqrt{1-\varepsilon_G}}{\varepsilon_G}. \tag{3.22}$$

Evaluating the bimodal Maxwell-Hewitt relation at $f_{large} = f_{max}$ and comparing the resulting relation with the monodisperse Maxwell-Hewitt relation enables determination of the maximum possible error in gas volume fraction, $(\Delta\varepsilon_G)_{max}$, as a function of true gas volume fraction, ε_G. The error $(\Delta\varepsilon_G)_{max}$ never exceeds 0.028, the value at $\varepsilon_G = 0.723$, and is less than 0.01 for $\varepsilon_G \leq 0.3$. Since this degree of uncertainty is comparable to the uncertainty of the monodisperse Maxwell-Hewitt relation itself, it appears that bubble-size distribution does not significantly affect the accuracy of the Maxwell-Hewitt relation.

3.3.4. Other Uncertainty Considerations

It is important to assess the degree to which uncertainties in experimental voltage measurements translate into uncertainties in the material distribution profiles reconstructed by EIT. Table 3.6 shows the fundamental voltage solution from the library file used by `EITAXI` that corresponds to conductivity parameter values of $C_0 = 1$, $C_1 = 0$, and $C_2 = 0$. Also shown are fundamental voltage solutions into which small errors have been deliberately introduced. Specifically, an error of 0.0001 (smaller than uncertainties seen from experimental projection sets with 25 measurements averaged per set) is added to the indicated voltage. These erroneous fundamental voltage solutions are used to create pseudo-experimental voltage projection sets that are subsequently analyzed by `EITAXI`.

Table 3.7 shows the values of the conductivity parameters that result from introducing these errors. Several observations can be made about these results. First, in the "no errors" case, `EITAXI` returns values of the conductivity parameters that are slightly different from the values used to create the projection set. The differences are acceptably small, below 10^{-3}, and are caused principally by the precision to which the voltages are written in the experimental voltage data file. Increasing this "experimental" precision reduces the differences substantially, although